Progress In Electromagnetics Research B, Vol. 114, 1–12, 2025

PIER B

(Received 12 March 2025, Accepted 9 July 2025, Scheduled 24 July 2025)

PSF-Based Antenna Array Optimization Method for Synthetic Aperture Interferometric Radiometer

Xinqian Chen[1], Yujie Ruan[1], and Jianfei Chen[1, 2, *]

[1] *College of Electronic and Optical Engineering and the College of Flexible Electronics (Future Technology)*
Nanjing University of Posts and Telecommunications, Nanjing 210023, China
[2] *State Key Laboratory of Millimeter Waves, Nanjing 210096, China*

ABSTRACT: The antenna array structure represents a pivotal technology for synthetic aperture interferometric radiometers (SAIRs). However, current array optimization metrics often have conflicting relationships among themselves, posing a significant challenge to achieving a harmonious balance. To tackle this issue, this paper introduces the point spread function (PSF) into the array optimization process and proposes a PSF-based antenna array optimization method. As a crucial characterization of the SAIR system, PSF can effectively evaluate the SAIR's comprehensive imaging performance. The mainlobe-sidelobe comprehensive quality (MSCQ) is innovatively proposed as a system-level metric to evaluate PSF quality and guide array optimization. The MSCQ consists of two parts: the main lobe width and side lobe energy ratio. The main lobe width can evaluate the spatial resolution of SAIR, and the side lobe energy ratio can evaluate the noise performance. In addition, in order to overcome the defect that the traditional optimization algorithm is prone to fall into the local optimum, this paper adopts the improved velocity-paused particle swarm algorithm (VPPSO) for high-precision optimization. The experimental results show that the PSF-based optimized array can effectively enhance SAIR's comprehensive performance and achieve high-performance imaging.

1. INTRODUCTION

Synthetic aperture interferometric radiometer (SAIR) overcomes the limitation of antenna physical aperture through synthetic aperture technology. Distinguished by its high resolution and robust anti-interference capability, it presents promising application prospects in fields such as Earth remote sensing and radio astronomy [1–3]. In essence, SAIR measures the target scene visibility function by performing a complex cross-correlation operation on the target scene radiation signals collected by antennas at distinct positions. Subsequently, a high-precision inversion method is employed to reconstruct the brightness temperature image of the target scene [4–6]. The antenna array plays a pivotal role in SAIR imaging. Its array structure determines the sampling distribution of the visibility function, which in turn directly affects the imaging performance of SAIR. Specifically, the antenna configuration is closely related to performance metrics such as spatial resolution, radiation sensitivity, and reliability, all of which collectively determine the overall imaging capability of SAIR—namely, its comprehensive imaging performance. This comprehensive performance is typically quantified by the quality of the reconstructed image (e.g., RMSE), providing a measurable reference for practical SAIR applications. This also indicates that optimizing the antenna array is a significant and necessary technique to enhance SAIR's comprehensive imaging performance.

Currently, there are many studies on optimizing the array configuration to improve the performance of SAIR. Spatial resolution as a key performance metric of SAIR can be improved by optimizing array redundancy [7]. By properly arranging antennas, the longest baseline (L) can be increased, thus effectively improving the SAIR's spatial resolution. The optimized low redundancy arrays (LRAs) obtained in this way have been a focal point of research efforts. Ref. [8] first achieved low redundancy linear arrays (LRLAs) with 12–30 array elements using simulated annealing. Subsequently, Dong et al. [9] and Jiang et al. [10] enhanced the optimization efficiency and derived more LRLA configurations by generalizing the model of LRLAs. Radiation sensitivity is another crucial performance metric of SAIR that cannot be overlooked. To address SAIR's radiation sensitivity, Dong et al. [11] proposed the degradation factor (DF) as an optimization metric. The minimum degradation arrays (MDAs) obtained by optimizing DF via simulated annealing can effectively improve the SAIR radiation sensitivity. Later, Zhu et al. [12, 13] proposed two determination methods for array arrangement based on DF. Additionally, Zhu et al. [14] explored an array design for SAIR reliability and introduced uncoverage factor (UCF) as an optimization metric. Zheng et al. [15] aimed at SAIR alias-free field-of-view optimization and obtained a large field of view linear array (LFOVLA) by heuristic algorithm and direct search. Notwithstanding these efforts, the existing optimization metrics and methods primarily concentrate on the array level, targeting individual performance metrics and aiming to enhance these specific metrics through array optimization. However, optimizing a single metric at the array level frequently has implications for other metrics. For example, LRLAs improve SAIR's spatial resolution by reduc-

---

* Corresponding author: Jianfei Chen (Chenjf@njupt.edu.cn).

doi:10.2528/PIERB25031203

Published by THE ELECTROMAGNETIC ACADEMY

ing redundancy but concomitantly lead to a loss of sensitivity [16]. Sensitivity is of particular significance for SAIR, especially in low-orbit Earth remote sensing, and thus must be carefully accounted for in array optimization [11]. Baseline redundancy, especially a uniformly distributed baseline, is the key to sensitivity enhancement [17]. Moreover, LRAs are less reliable due to their low redundancy [14]. SAIR's imaging performance may degrade significantly in the event of antenna damage. In practice, moderately sparse arrays are often preferred over LRLA [18, 19]. In summary, SAIR array optimization is a complex problem that necessitates the comprehensive consideration of multiple factors. Optimizing a single metric alone is insufficient to achieve the best comprehensive imaging performance; instead, a balance must be struck among various performance indicators. Zhu et al. [14] proposed a multi-objective optimization framework to jointly optimize L, DF, and UCF. However, the resulting solution is a set of Pareto-optimal arrays, which still requires subjective selection of the best configuration. In addition, Zhu et al. [20] introduced the BlockMFRA method, which structurally optimizes the trade-off between sensitivity and resolution. Nevertheless, this method essentially remains within the multi-objective optimization paradigm, and the final configuration still depends on specific task requirements. Existing research on array optimization mainly focuses on optimizing array-level metrics, but the inherent trade-offs among different indicators make it difficult to satisfy all performance requirements simultaneously. Therefore, an effective system-level metric is needed to guide the optimization for the best comprehensive imaging performance of SAIR.

In response, this paper, based on the analysis of PSF as an important characterization of the SAIR system function, considers that PSF can accurately map multiple system characteristics and is a key indicator reflecting the comprehensive system performance. Based on this, a novel PSF-based antenna array optimization method is proposed, which can effectively enhance the system's comprehensive performance and achieve high-quality imaging. It innovatively proposes mainlobe-sidelobe comprehensive quality (MSCQ) as a system-level metric for evaluating PSF's comprehensive quality, guiding antenna array optimization. MSCQ comprises two components: the main lobe width and the side lobe energy ratio (ER). Main lobe width assesses PSF main lobe quality. Linked to the SAIR visibility function's uv coverage, it characterizes SAIR spatial resolution; a narrower width implies higher resolution. ER evaluates PSF side lobe energy, reflecting noise interference in SAIR imaging. A larger ER means lower side lobe energy and less noise in the reconstructed image. It also implies higher main lobe energy and better system radiation sensitivity. MSCQ introduces an adjustment factor α to balance the weights between main lobe and side lobe metrics, flexibly meeting different optimization requirements. In the optimization process, side lobe energy ratio is taken as the primary optimization target, while main lobe width is also controlled. Therefore, α is usually set to a smaller value to enhance the suppression of side lobe energy. Considering the importance of spatial resolution, for array structures with relatively small uv coverage, α is appropriately increased to reduce their impact during optimization, thereby protecting SAIR's spatial resolution. Moreover, the optimization process employs the new velocity pause particle swarm optimization (VPPSO) algorithm [21] for high-precision optimization. VPPSO includes a constant-velocity option and modifies velocity update formulas, balancing exploration and exploitation to avoid premature convergence common in classical particle swarm algorithms. It also uses a two-population strategy to maintain particle-population diversity. Simulated experiments show that PSF-based antenna array optimization method can achieve a good balance among multiple performance metrics, such as spatial resolution, radiation sensitivity, and imaging reliability, significantly enhancing SAIR's comprehensive performance and imaging quality. Furthermore, the method is applicable to both one-dimensional and two-dimensional array structures, compensating for the current lack of sufficient research in two-dimensional array optimization.

2. PSF-BASED ANTENNA ARRAY OPTIMIZATION METHOD

To enhance the comprehensive performance of SAIR, this paper presents a novel PSF-based array optimization method. This method incorporates PSF into the array optimization process. A comprehensive evaluation metric for PSF is established and employed as the fitness function, with its values being fed back to guide the adjustment of array coordinates. The entire optimization process is executed through the application of a heuristic algorithm.

2.1. PSF Evaluation Metric

In the field of SAIR imaging, the PSF accurately describes the SAIR response to point sources. Through further analysis of SAIR imaging principles, the SAIR imaging process for a real target essentially constitutes a convolution operation between the real target image and PSF. As such, PSF can be considered as a system function of SAIR, playing an irreplaceable role in the comprehensive evaluation of SAIR's imaging performance. By conducting a profound analysis of PSF characteristics, one can effectively infer the relevant features of the final SAIR imaging outcomes. Notably, the evaluation results of the PSF are determined solely by the inherent characteristics of SAIR and remain immune to interference from changes in the original scene, endowing it with remarkable generalizability. Given the distinctive advantages of the PSF in SAIR imaging performance evaluation, this paper innovatively incorporates PSF into antenna array optimization process and proposes a PSF-based array optimization method.

PSF typically comprises two components: main lobe and side lobe. Main lobe represents the primary response of the imaging system to a point source. The width of main lobe reflects the diffusion of the system to the point source, which can be used to characterize the spatial resolution of the SAIR. The spatial resolution of SAIR, as an extremely critical performance metric, must be taken into account when array optimization is conducted. In general, the narrower the PSF main lobe width is, the higher the spatial resolution of SAIR is. As shown in Fig. 1, the pre-optimization array exhibits a relatively wide main lobe, resulting in low spatial resolution and poor

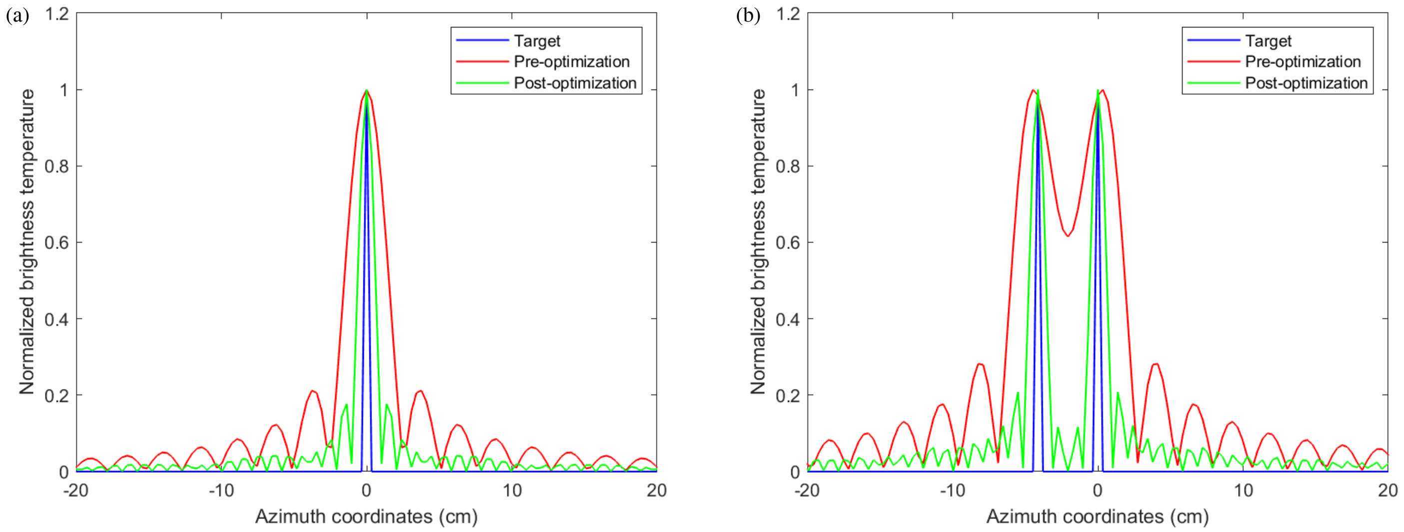

FIGURE 1. Plot of main lobe width versus resolution. (a) Images of the PSF. (b) Double point sources imaging results.

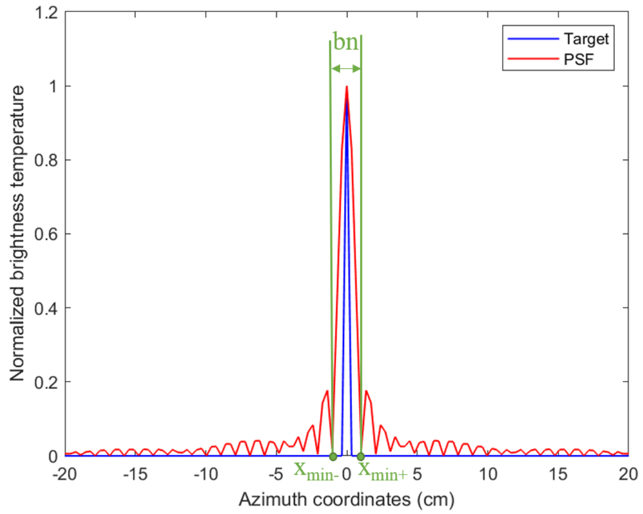

FIGURE 2. Main lobe width of 1D array.

ability to distinguish between two adjacent point sources. In contrast, the PSF-optimized array demonstrates a significantly narrower main lobe, thereby improving the spatial resolution and enabling the system to clearly and accurately resolve the two adjacent point sources. Therefore, the PSF main lobe width and SAIR spatial resolution have a clear correspondence, which can be used as an effective metric to characterize the spatial resolution of SAIR. For a 1D linear array, as depicted in Fig. 2, main lobe width can be defined as the width from the peak of the main lobe to the first minima. Mathematically, its expression is:

$$b_n = x_{\min+} - x_{\min-} \tag{1}$$

For 2D arrays, the PSF's main lobe is the most luminous planar region at its center. Its geometric configuration exerts a profound influence on the imaging performance of the SAIR. When the main lobe exhibits symmetry in a circular form, the reconstructed image can more accurately replicate the original shape of the target; conversely, an asymmetric, elliptical main lobe will lead to corresponding geometric distortion in the reconstructed image. As shown in Fig. 3, the pre-optimization array exhibits obvious asymmetry in the main lobe, causing severe geometric distortion in the reconstructed image; however, after PSF-based optimization, this asymmetry is significantly reduced, and the geometric distortion in the reconstructed image is correspondingly improved. Therefore, when assessing the main lobe width of a 2D-array PSF, it is essential to not only consider the lengths of the main lobe's major and minor axes but also comprehensively evaluate the symmetry between these axes. As illustrated in Fig. 4, the mathematical expression for this is:

$$b_n = \frac{\max(a(n), b(n))}{\min(a(n), b(n))} \times \frac{a(n) + b(n)}{2} \tag{2}$$

where $a(n)$ represents the span of the main lobe's long axis, and $b(n)$ represents the span of the main lobe's short axis. The ratio $\frac{\max(a(n),b(n))}{\min(a(n),b(n))}$ serves as a metric for quantifying the symmetry of the main lobe. The closer this ratio is to 1, the more similar the lengths of the main lobe's long and short axes become, indicating better symmetry of the main lobe. This enhanced symmetry is more conducive to SAIR's accurate target shape reconstruction performance.

On the other hand, PSF side lobe determines the noise interference in the actual SAIR imaging process, which is an important piece of information to measure the comprehensive imaging performance of SAIR. Given the essential nature of the SAIR imaging process, when the energy of the PSF is concentrated, and the side lobe energy is low, the final reconstructed image experiences minimal noise interference and is highly distinct. Conversely, when PSF energy is dispersed, and side lobe energy is high, the final reconstructed image is marred by substantial background noise and appears blurred. As shown in Fig. 5, compared with pre-optimization PSF, post-optimization

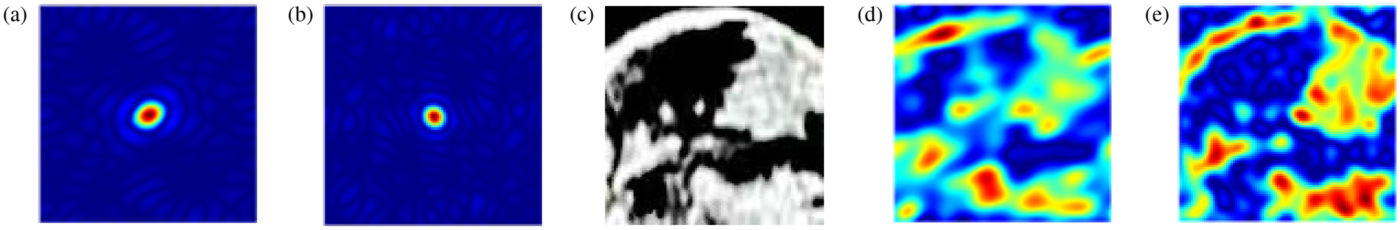

FIGURE 3. Plot of main lobe shape versus imaging deformation. (a), (b) Images of the PSF. (c)–(e) Original target image and reconstructed image of the remote sensing. (a) Pre-optimization PSF, (b) Post-optimization PSF, (c) Remote sensing, (d) Pre-optimization RS, and (e) Post-optimization RS.

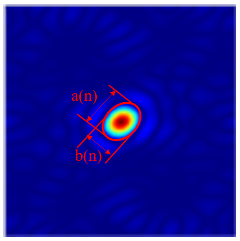

FIGURE 4. Main lobe width of 2D array.

PSF exhibits significantly lower side lobe levels, which correspondingly leads to reduced noise interference in the imaging of real target scenes. Thus, this paper innovatively introduces a key parameter, PSF side lobe energy ratio (ER). ER serves mainly to evaluate the state of the PSF side lobe and to quantify the degree of noise interference within the SAIR system's imaging process. The definition of ER is illustrated in Fig. 6. Specifically, the integration region of the main lobe is defined as the area from the PSF peak to the first minima, while the side lobe integration region refers to the areas on both sides of the main lobe where the amplitude gradually decays. ER is defined as the ratio of the PSF's main lobe energy to its side lobe energy. Its mathematical expression is:

$$ER = \frac{\sum_{\text{mainlobe}} S(n)}{\sum_{\text{others}} E(n)} \tag{3}$$

In this formula, $S(n)$ represents the main lobe energy, and $E(n)$ represents the side lobe energy. A larger ER value indicates that the energy of the PSF is more concentrated, with higher main lobe energy and lower side lobe energy. Correspondingly, the final reconstructed image will have less background noise and better image clarity, and the system will have better sensitivity.

Taking into account all the characteristics of the PSF, the comprehensive performance of the PSF can be evaluated using mainlobe-sidelobe comprehensive quality (MSCQ) as follows:

$$\text{MSCQ} = |\alpha b_n - ER| \tag{4}$$

where ER is as in Eq. (3), and bn is calculated as in Eq. (1) for 1D array optimization and Eq. (2) for 2D array optimization. α is the adjustment factor, which can be adjusted according to the actual optimization demand. In this paper, ER optimization is the main focus, so the overall setting of α value is smaller. For arrays with small uv coverage, increasing α appropriately can reduce its influence in the optimization, thus helping to ensure SAIR's spatial resolution.

2.2. SAIR Imaging Principles

SAIR can obtain its PSF by inverse imaging of a single point source. The fundamental structure of SAIR is a binary interferometer as shown in Fig. 7. It can obtain the visibility function by complex correlation operation of radiation signals received from antennas at different locations. Subsequently, a high-precision inversion algorithm can be utilized to invert the bright temperature image of the target from the visibility function.

Ideally, the following relationship exists between the measured visibility function and the bright temperature distribution of the target scene, which is the basis for the inversion process proposal [22]:

$$\begin{aligned} V_{c,l} &= < E_c(t) \cdot E_l^*(t) > \\ &= \sum_{n=0}^{N} T(n) F_c(x_n, y_n) F_l^*(x_n, y_n) e^{-iK(R_n^c - R_n^l) d\Omega} \end{aligned} \tag{5}$$

where $E_c(t)$ and $E_l(t)$ are the scene radiation signal received by antenna c and l; F_c and F_l are the normalized antenna direction maps; (x_n, y_n) is the coordinates of the radiation source at the n-th point; T is the normalized brightness temperature; $d\Omega$ is the steradian angle that the radiating source S opens to the antenna. The wave range difference obtained by subtracting the R_n^c and R_n^l is a very critical part, which according to Fig. 7 can be specifically expressed as:

$$R_n^c = \sqrt{(x_n - X_c)^2 + (y_n - Y_c)^2 + R^2} \tag{6}$$

$$R_n^l = \sqrt{(x_n - X_l)^2 + (y_n - Y_l)^2 + R^2} \tag{7}$$

where $X_\#$, $Y_\#$ are the position coordinates of antenna #. Typically, a Taylor expansion of the distances R_n^c, R_n^l is required for variable separation and substituted back into Eq. (5). Then rewrite Eq. (5) into the following matrix form:

$$V_{M\times 1} = G_{M\times N} T_{N\times 1} \tag{8}$$

where V is the vector form of the visibility matrix, G the system matrix or imaging operation matrix, and T the vector form of the bright temperature image.

$$G(m,n) = F_c(x_n, y_n) F_l^*(x_n, y_n) e^{i\pi(R_n^l - R_n^c)/\lambda} \tag{9}$$

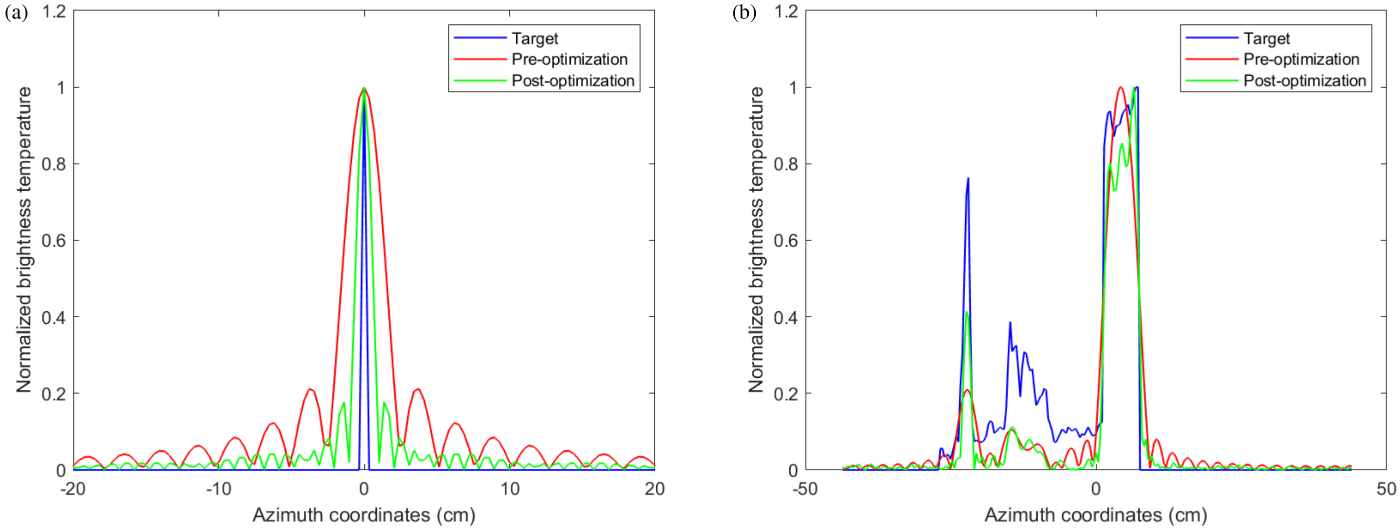

FIGURE 5. Plot of side lobe versus noise interference. (a) Images of the PSF. (b) Real target imaging results.

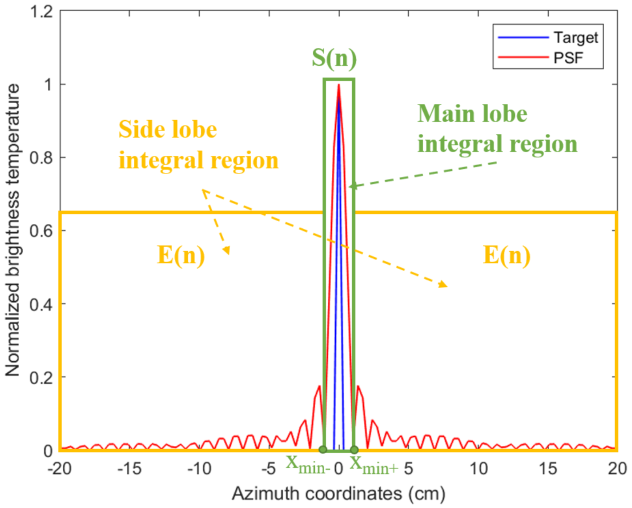

FIGURE 6. Schematic of ER.

where m represents the m-th spatial sampling point, and n represents the n-th target point pixel value to be recovered in the imaging region. After obtaining the expression of the G matrix, the image T can be obtained by solving the inverse problem of Eq. (8) using FISTA [23]. The G-matrix imaging method can be directly used for arbitrarily shaped arrays, which is suitable for the use in array optimization. In addition, it inverts the target image directly from the measured visibility function, avoiding the introduction of additional errors and thus ensuring higher inversion imaging accuracy.

2.3. Optimization Algorithm

Particle swarm optimization algorithm (PSO) [24] is a group intelligence-based optimization algorithm which is easy to implement and has fast convergence speed. It has shown excellent performance in solving various types of optimization problems, including array optimization problems [10]. However, PSO still suffers from inherent shortcomings such as slow late-stage convergence and tendency to fall into local optimization. In addition, array optimization is a high-dimensional optimization problem, and PSO tends to suffer performance degradation when handling such high-dimensional optimization problems. Therefore, a new velocity pause particle swarm optimization (VPPSO) algorithm [21] is selected for array optimization to improve the optimization performance, and the specific flowchart is shown in Fig. 8. It uses a two-population model to increase particle diversity. On the other hand, it adjusts the particle position and velocity updating formula to avoid the particles converging prematurely.

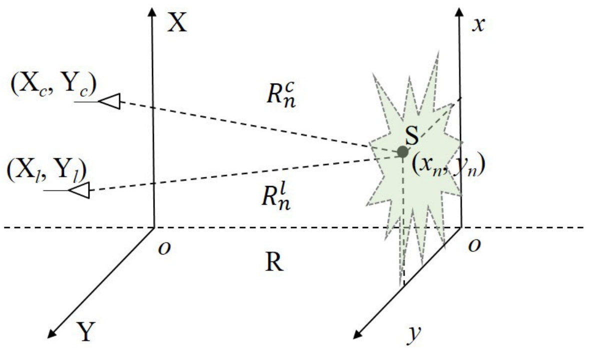

FIGURE 7. Schematic diagram of binary interferometry.

In traditional PSO, particles can only choose to move at slower or faster speeds in each iteration. In contrast, VPPSO increases the possibility of the particles to move at the same speed as the previous iteration, which helps to balance the exploration and exploitation process and avoids the particles from converging prematurely. Therefore, the speed is updated as:

$$V_i(t+1) = \begin{cases} V_i(t) & \text{if rand} < \beta \\ V_i(t+1) & \text{Otherwise} \end{cases} \tag{10}$$

where β is a constant. A random number is used to determine a portion of the particles to keep their original velocity

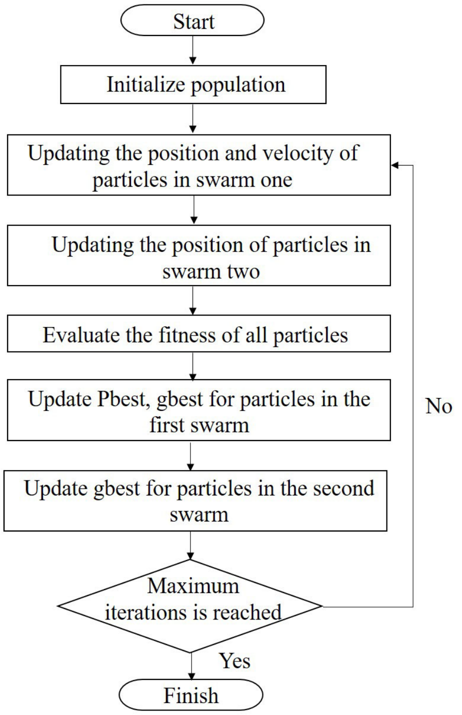

FIGURE 8. VPPSO flowchart.

unchanged, and the remaining particles undergo a velocity update. Also, to further avoid premature convergence, the VPPSO changes the first term in the traditional PSO velocity update formula. The altered particle velocity update formula is as follows:

$$\begin{aligned} V_i(t+1) = & V_i(t)^{r_1 a(t)} + c_1 r_2 (Pbest(t) - X_i(t)) \\ & + c_2 r_3 (gbest(t) - X_i(t)) \end{aligned} \tag{11}$$

where r_1, r_2, r_3 are random numbers within [0, 1]; Pbest is individual optimization, gbest is group optimization; c_1, c_2 are the individual cognitive coefficient and social cognitive coefficient, respectively, which are usually set as constants. The expression of $a(t)$ is shown below:

$$a(t) = \exp - \left(\frac{bt}{T} \right)^b \tag{12}$$

where b is a constant, t the current iteration round, and T the maximum iteration. In order to increase the diversity of particles, the VPPSO also divides the N particles into two populations with different particle position updating methods. The particles in the first population $N1$ update their positions according to the traditional PSO mechanism. The particles in the second population $N2$ update the position only based on the population optimum. Therefore, the position update formula of the particles is as follows:

$$i \in N1: X_i(t+1) = X_i(t) + V_i(t+1) \tag{13}$$

$i \in N2:$

$$X_i(t+1) = \begin{cases} gbest + a(t) r_4 |gbest|^{a(t)} & \text{if } r_5 < 0.5 \\ gbest - a(t) r_6 |gbest|^{a(t)} & \text{Otherwise} \end{cases} \tag{14}$$

where $V_i(t+1)$ is updated according to Eq. (10), ans r_4, r_5, r_6 are random numbers within [0, 1]. When VPPSO is applied to an array optimization problem, each particle X represents a set of independent array arrangements. An array arrangement containing n array elements is represented as an n-dimensional vector:

$$X = [x_1, x_2, \cdots, x_n] \tag{15}$$

where x_i denotes the coordinate position of the i-th antenna. In the optimization process, the fitness function is chosen as Eq. (4).

3. EXPERIMENTS AND RESULTS ANALYSIS

To validate the effectiveness of the PSF-based array optimization method, this section conducts 1D and 2D array optimization experiments. Its optimized simulation model is shown in Fig. 9.

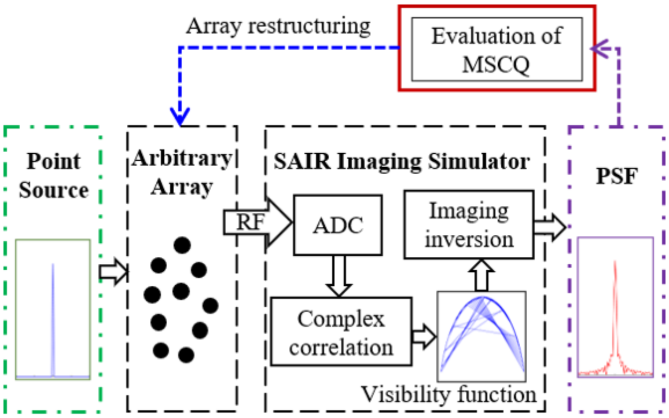

FIGURE 9. Optimized simulation model block diagram.

In the experiment, the point source target signals are firstly acquired by the array elements, and the visibility function is obtained by complex correlation operation of the point source signals acquired by the array elements. The PSF is then inverted using the G-matrix based imaging method described in Subsection 2.2, and finally, the PSF is evaluated by calculating the MSCQ, and the results are used to guide the adjustment of the array structure, thus forming a complete feedback optimization loop. The whole optimization process is realized by the optimization algorithm of VPPSO introduced in Subsection 2.3.

3.1. 1D Array Optimization Experiments

For the 1D sparse array optimization, a fixed number of antennas ($M = 18$) is utilized to ensure complete uv coverage. The population size of VPPSO is set to 50, and the number of iteration rounds to 200. Considering the effect of resolution on the optimization results and SAIR performance, α in Eq. (4) is adjusted. $bn >= 6$ is set to $\alpha = 0.08$, and $\alpha = 0.001$ for the rest of the cases. To demonstrate the effectiveness of the optimization, we compared and evaluated the optimized array MSCQ-A with commonly used optimized array configurations filled linear array (FLA), LRLA, and twofold redundancy linear array (TFRLA) [25] based on numerical metrics and simulated

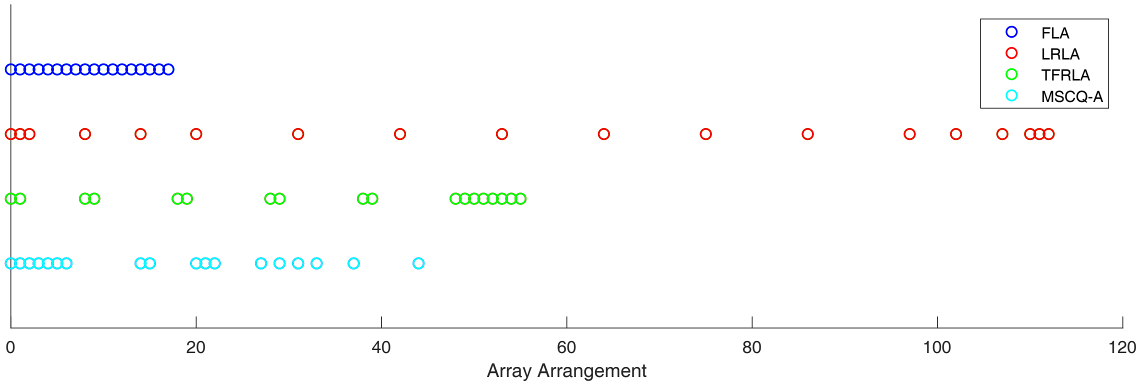

FIGURE 10. Array layout diagram.

imaging quality. The array element structures of these arrays are shown in Fig. 10.

Table 1 summarizes the results of the numerical comparisons, which include metrics such as redundancy, DF [11], and UCF [14].

TABLE 1. 1D array comparison.

ARRAY	L	R	DF	UCF	MSCQ
FLA	17	9	1.317	0.1	0.267
LRLA	112	1.366	7.049	10.1	0.320
TFRLA	55	2.781	3.476	0.2	0.625
MSCQ-A	44	3.477	3.133	1.2	0.993

As can be seen from the table, MSCQ-A array significantly outperforms the other arrays in terms of PSF quality. Compared with LRLA, which aims for low redundancy, MSCQ-A, despite having relatively higher redundancy, demonstrates superior sensitivity and reliability. TFRLA attempts to achieve low redundancy while maintaining double redundancy, thereby improving reliability to some extent. However, it still has limitations in sensitivity. FLA, although it possesses certain advantages in sensitivity and reliability, suffers from poor resolution due to its higher redundancy. Notably, in addition to having the best PSF quality, MSCQ-A exhibits a more balanced performance across the remaining performance metrics, indicating a better compromise among different aspects of performance. To further verify the effectiveness of the optimization, we performed simulated imaging experiments.

In Fig. 11, the PSF, the imaging results of the ideal image, and the imaging results of a typical real-scene image for each array are presented in sequence. Here, the blue color represents the target image, and the red color represents the reconstructed image. First, Figs. 11(a)–(d) display the PSF of each array. In the imaging domain, the baseline length is closely correlated with the resolution. Generally speaking, the longer the baseline is, the higher the resolution is. Among this set of arrays, LRLA has the longest baseline, resulting in the narrowest main lobe width and the best resolution. Conversely, FLA has the shortest baseline, leading to the widest main lobe width, the poorest resolution, and a more prominent and larger side lobe. The difference in baseline lengths between the MSCQ-A and TFRLA is relatively small. Thus, the widths of their main lobes are similar; their resolutions are at an intermediate level; and neither shows a significant side lobe. Notably, MSCQ-A features a more concentrated main lobe, more complete main lobe shape, and narrower first side-lobe width with a lower amplitude. Figs. 11(e)–(h) display the imaging results of an ideal rectangle and a triangle. The imaging results of the FLA largely preserve the basic shape of the rectangle, but it exhibits slight undulations at the edges. LRLA has the advantage of high resolution, and yet it introduces excessive noise when processing smooth, large-scale targets, leading to severe image distortion. In contrast, MSCQ-A and TFRLA can better reproduce the image shape with lower background noise levels. For a more in-depth comparison, MSCQ-A shows less fluctuation than TFRLA in the rectangular region and smoother edges in the triangular region, resulting in superior imaging results. Figs. 11(i)–(l) present the real target imaging results. Due to its lower resolution, the FLA loses a significant amount of image details, and the height and shape of the target wave peaks are notably diminished. The LRLA restores the wave-peak energy relatively well, but simultaneously, it introduces more high-frequency noise, which increases the sharpness of the wave peaks. The noise on both sides is obvious and affects the overall imaging quality. The MSCQ-A and TFRLA have similar resolutions, and they both perform well in restoring the single targets on the left side. They also have similar capabilities in controlling background noise. However, the MSCQ-A outperforms in reproducing the shape of the weak-target region in the middle of the image. In the concentrated high-target region on the right side, the MSCQ-A can better reproduce the energy, basically restoring the energy and detailed information of the original image. In terms of the numerical metric root-mean-square error (RMSE), the RMSE of the MSCQ-A reconstructed images has a clear advantage, both for ideal and actual targets. In conclusion, the characteristics of the imaging results of both the ideal and actual images are consistent with those reflected by the PSF. Through quantitative and qualitative evaluations, it has been confirmed that MSCQ-A can assist SAIR in achieving better overall performance and higher-performance imaging. This further validates the effectiveness of the PSF-based array optimization method.

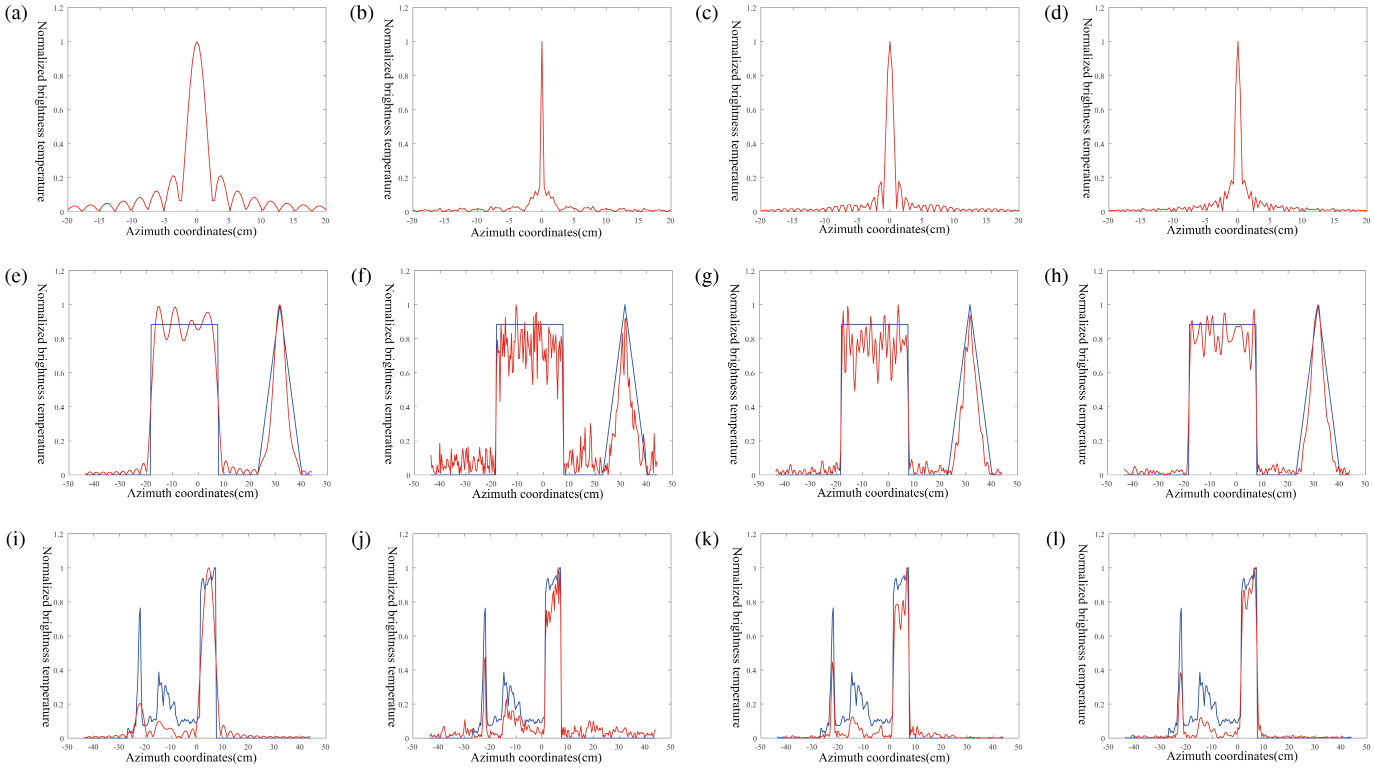

FIGURE 11. 1D array imaging image. (a)-–(d) Images of the PSF. (e)-–(h) Ideal target imaging results. (i)-–(l) Real target imaging results. (a) FLA PSF, (b) LRLA PSF, (c) TFRLA PSF, (d) MSCQ-A PSF, (e) FLA RMSE = 0.1067, (f) LRLA RMSE = 0.1487, (g) TFRLA RMSE = 0.1117, (h) MSCQ-A RMSE = 0.0912, (i) FLA RMSE = 0.1070, (j) LRLA RMSE = 0.0842, (k) TFRLA RMSE = 0.0850, and (l) MSCQ-A RMSE = 0.0791.

3.2. 2D Array Optimization Experiments

To further validate the effectiveness of the PSF-based array optimization method, a series of 2D experiments were conducted. Experiments were conducted for array configurations with a fixed number of antennas ($M = 30$). The population size of VPPSO was set to 50, and the number of iteration rounds was 200. Considering the influence of resolution on the optimization results and the performance of SAIR, when $bn >= 18$ in Eq. (4), $\alpha = 0.001$ was set, and in other cases, $\alpha = 0.015$. Simulated imaging experiments were performed and compared between the optimized MSCQ-A and commonly used U-shaped, Y-shaped, and circular arrays.

In Figs. 12(i)–(l), the PSFs of different arrays are presented, which show a significant correlation with their corresponding uv coverage. For the U-shaped array, due to the distribution characteristics of the rectangular sampling method in the spatial frequency domain, the energy diffuses both laterally and longitudinally around the main lobe. As a result, obvious lateral and longitudinal side lobes are presented in its PSF image. The Y-shaped array adopts a hexagonal sampling pattern, and thus the distribution of sampling points has a certain symmetry. Its PSF exhibits distinct star-shaped side lobes. The circular array with a circular uv coverage shows circular interference fringe patterns in its PSF. The layout of MSCQ-A lacks regularity. This leads to less background noise in its PSF, and there is no obvious regular pattern. The irregular array layout reduces the periodic interference caused by regular structures, thereby reducing the background noise level.

In the imaging results of actual objects shown in Fig. 13, the performance of each array is consistent with its PSF characteristics. In the reconstruction images of the plane scene depicted in Figs. 13(b)–(e), regular interference noise appears in the background of the U-shaped array, Y-shaped array, and circular array reconstructed images. Among them, the noise interference of the Y-shaped and circular arrays has a negative impact on the restoration of the object's shape, resulting in distortion of the object. This is because the side lobe characteristics in their PSFs introduce additional interference during the imaging process, destroying the original shape information of the object. In contrast, MSCQ-A has less background noise and a clearer contour, demonstrating better image fidelity. Figs. 13(g)–(j) are the more complex remote sensing (RS) images. Due to the limitations of simulation conditions and the reduction in the number of array elements used, the imaging quality is affected to some extent. Even so, the contour of the islands in MSCQ-A image is still clearer and basically consistent with the original image. Moreover, for some faint small islands, MSCQ-A can also restore them well with less interference from noise, and it performs excellently in terms of retaining image details. The advantages of MSCQ-A are reflected in the imaging process, effectively reducing the interference of noise on the image and more accurately restoring the contour and detailed information. Table 2 presents a numerical comparison of the quality of

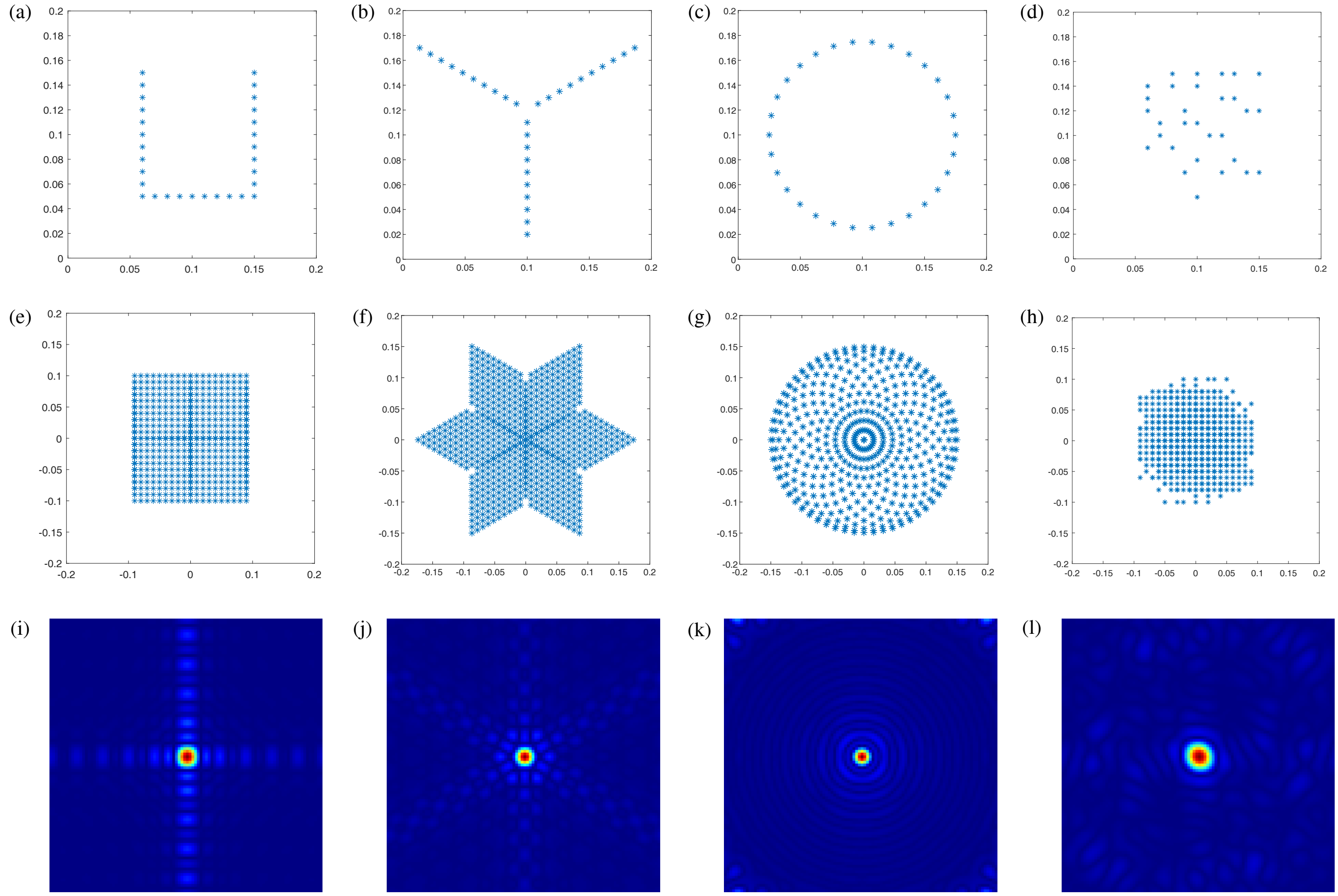

FIGURE 12. 2D array arrangement image. (a)–(d) Array layout. (e)–(h) uv coverage. (i)–(l) Images of the PSF. (a) U, (b) Y, (c) Circular, (d) MSCQ-A, (e) U uv, (f) Y uv, (g) Circular uv, (h) MSCQ-A uv, (i) U PSF, (j) Y PSF, (k) Circular PSF, and (l) MSCQ-A PSF.

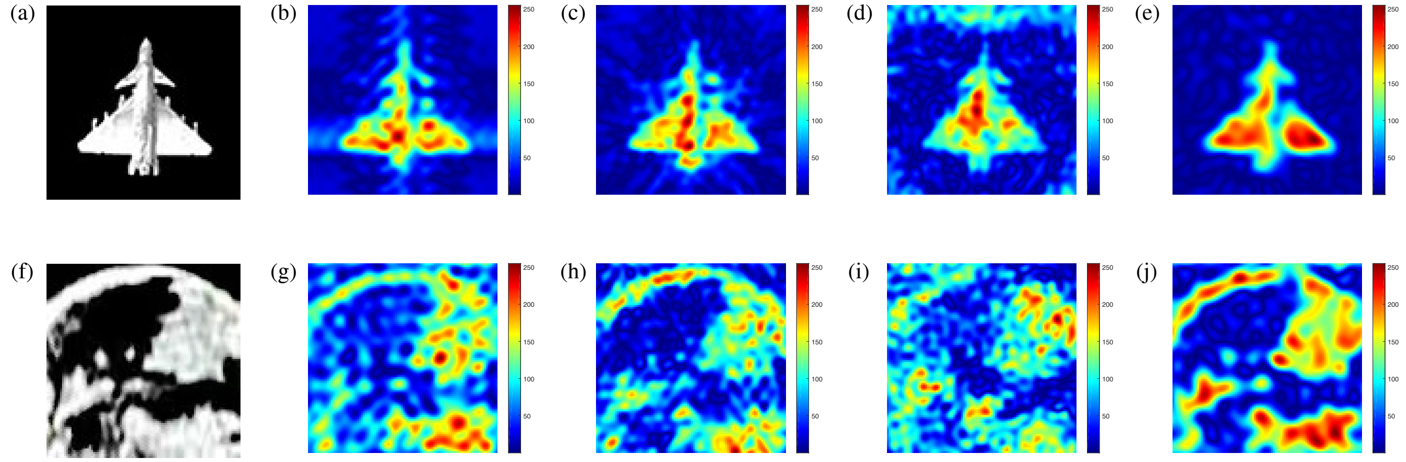

FIGURE 13. 2D scene reconstructed image. (a)–(e) Original target image and reconstructed image of the plane. (f)–(j) Original target image and reconstructed image of the remote sensing. (a) Plane Scene, (b) U Plane, (c) Y Palne, (d) Circular Plane, (e) MSCQ-A Palne, (f) Remote Sensing, (g) U RS, (h) Y RS, (i) Circular RS, and (j) MSCQ-A RS.

each image. By calculating the three main indicators, namely RMSE, peak signal-to-noise ratio (PSNR), and structural similarity index measure (SSIM), it can be seen from the numerical comparison results that MSCQ-A has the best imaging quality, which is consistent with the results of the image comparison.

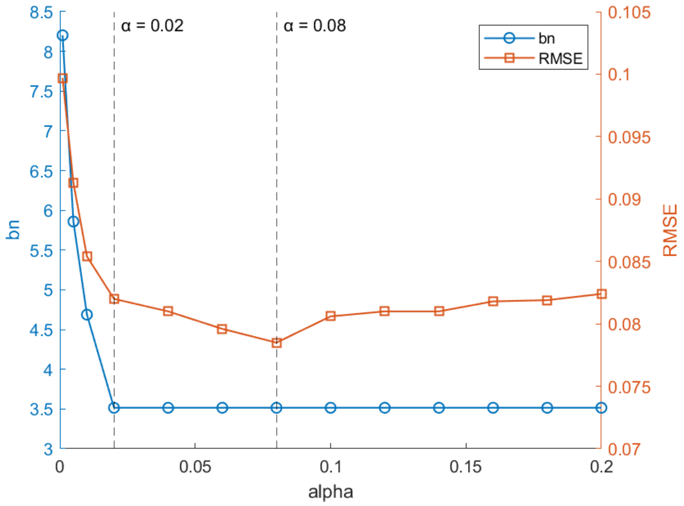

FIGURE 14. Plot of bn and RMSE versus adjustment factor α.

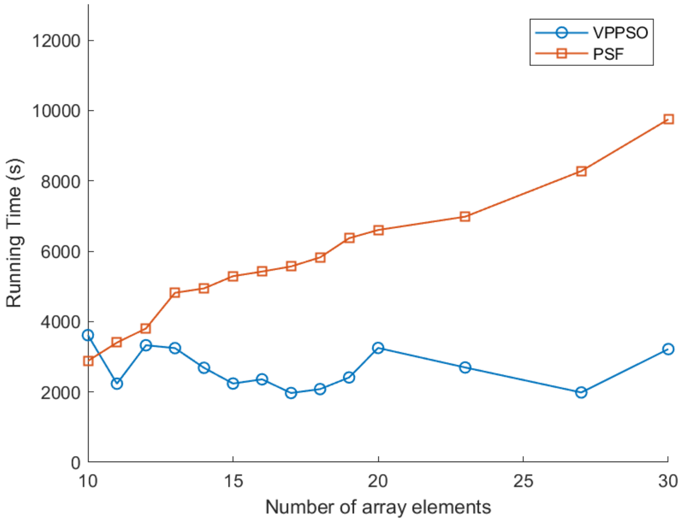

FIGURE 15. Optimization time and PSF imaging time of 1D arrays with different numbers of antennas.

TABLE 2. Comparison of imaging quality metrics.

Metrics		U	Y	Circular	MSCQ-A
Plane	PSNR	14.3504	14.7477	12.4325	15.7313
	RMSE	0.0756	0.0707	0.1999	0.0640
	SSIM	0.0781	0.0867	0.0752	0.0939
RS	PSNR	9.8559	9.6590	8.7978	11.5478
	RMSE	0.0693	0.0722	0.1147	0.0691
	SSIM	0.1470	0.1765	0.1107	0.2235

3.3. Comparison of 1D and 2D Array Optimization

Based on the previous experimental analyses of 1D and 2D array optimization, it is evident that different sampling geometries produce PSFs with distinct features, resulting in varied imaging performances. For 1D arrays, the main lobe width and side lobe amplitude determine resolution and noise interference, making these two metrics the focus of optimization analysis. The PSF structure of 2D arrays is more complex and often includes interference fringes and other regular noise patterns, which cannot be fully assessed by main lobe and side lobe parameters alone; therefore, optimization analysis focuses more on examining the distribution characteristics of these interferences. Although the structures differ, all experiments consistently indicate that the imaging results closely correspond to the PSF characteristics. The PSF-based array optimization method significantly improves the overall imaging quality of the SAIR system, as confirmed by quantitative metrics such as RMSE, PSNR, and SSIM, as well as visual results.

3.4. Sensitivity Analysis of Adjustment Factor α

Based on the previous optimization experiment of an 18-element 1D linear array, α is set to 0.08 when the condition $bn >= 6$ is met; otherwise, it is set to 0.001. This strategy achieved relatively ideal optimization results. However, the optimization performance still depends, to some extent, on the specific value of α. Therefore, this paper further investigates the impact of different α values on the optimization results.

Since the optimization mainly focuses on ER and secondarily on bn, α should be kept relatively small to emphasize side lobe suppression. For arrays with good uv coverage, a small α (e.g., 0.001) helps improve ER without significantly affecting main lobe control. However, when uv coverage is insufficient, an excessively small α may fail to effectively converge the main lobe width, leading to decreased spatial resolution, increased RMSE, and a significant decline in overall imaging quality. To this end, this paper tests α values ranging from 0.001 to 0.2 for arrays with insufficient uv coverage. As shown in Fig. 14, when α is too small (less than 0.02), the system exhibits weak regulation of the main lobe width, resulting in poor convergence of the main lobe, low spatial resolution, and significantly increased RMSE. As α increases, the system's optimization weight on the main lobe grows, the main lobe width gradually narrows; RMSE significantly decreases; and spatial resolution improves. Notably, at $\alpha = 0.08$, the system achieves a good balance between side lobe suppression and main lobe control, yielding the best overall imaging performance.

In summary, the experiments validate the effectiveness of using $\alpha = 0.08$ in the optimization of the 1D linear array. This value suppresses side lobe energy while maintaining good control over the main lobe width, avoiding resolution degradation and demonstrating superior overall imaging performance.

3.5. Algorithm Time Performance Analysis

This paper presents a statistical analysis of the optimization time and PSF imaging time for 1D arrays with different numbers of antennas. Specifically, incremental tests were conducted for arrays with 10 to 20 antennas, while for arrays with more than 20 antennas, intermittent sampling was performed due to time constraints, as shown in Fig. 15. The results indicate that as the number of antennas increases, the PSF computation time grows significantly, reflecting that its complexity is positively correlated with the number of antennas, which aligns with theoretical expectations. In contrast, the overall runtime of the VPPSO optimization algorithm shows little change and exhibits some fluctuations, which may be attributed to the stochastic nature of the algorithm. This phenomenon demonstrates that VPPSO can rapidly converge to the global optimum and possesses good scalability and stability, with its performance hardly affected by the increase in the number of antennas.

4. CONCLUSIONS

This paper innovatively proposes a PSF-based antenna array optimization method for SAIR. The method integrates the PSF into an array optimization process, leveraging the main lobe and side lobe of the PSF to evaluate system resolution, noise interference, sensitivity, etc. Based on this, a system-level optimization metric, MSCQ, is proposed to assess the comprehensive performance of SAIR and guide array optimization. During the optimization process, VPPSO algorithm is adopted to achieve precise optimization and improve optimization efficiency. Experimental verification shows that PSF-based array optimization method demonstrates excellent applicability in both 1D and 2D array optimizations. Compared with traditional arrays, the optimized MSCQ-A maintains an appropriate degree of redundancy, sensitivity, and reliability, achieving a good balance in all aspects of performance. Notably, MSCQ-A significantly improves the imaging quality of SAIR, endowing SAIR with higher comprehensive performance and high-performance imaging results, thus validating the effectiveness and feasibility of the PSF-based method. This study provides new insights for SAIR array optimization.

ACKNOWLEDGEMENT

This work was supported in part by the National Natural Science Foundation of China under Grant No. 62371255 and No. 61601237, in part by the China Postdoctoral Foundation under Grant No. 2017M621585, in part by the Millimeter-wave State Key Laboratory Open project grant No. K202526.

REFERENCES

[1] Arras, P., P. Frank, P. Haim, J. Knollmüller, R. Leike, M. Reinecke, and T. Enßlin, "Variable structures in M87* from space, time and frequency resolved interferometry," *Nature Astronomy*, Vol. 6, No. 2, 259–269, 2022.

[2] Li, Y., X. Yin, W. Zhou, M. Lin, H. Liu, and Y. Li, "Performance simulation of the payload IMR and MICAP onboard the Chinese ocean salinity satellite," *IEEE Transactions on Geoscience and Remote Sensing*, Vol. 60, 1–16, 2021.

[3] Fu, P., D. Zhu, F. Hu, Y. Xu, and H. Xia, "A near-field imaging algorithm based on angular spectrum theory for synthetic aperture interferometric radiometer," *IEEE Transactions on Microwave Theory and Techniques*, Vol. 70, No. 7, 3606–3616, 2022.

[4] Zhang, Y., Y. Ren, W. Miao, Z. Lin, H. Gao, and S. Shi, "Microwave SAIR imaging approach based on deep convolutional neural network," *IEEE Transactions on Geoscience and Remote Sensing*, Vol. 57, No. 12, 10 376–10 389, 2019.

[5] Anterrieu, E. and L. Yu, "Impact of the antenna spacing on the brightness temperature maps retrieved with a synthetic aperture imaging radiometer," *Remote Sensing*, Vol. 15, No. 3, 805, 2023.

[6] Wu, Y., Y. Li, G. Song, H. Dou, D. Wen, P. Li, X. Yang, R. Lv, and H. Li, "A near-field imaging method based on the near-field distance for an aperture synthesis radiometer," *Remote Sensing*, Vol. 16, No. 5, 767, 2024.

[7] Moffet, A., "Minimum-redundancy linear arrays," *IEEE Transactions on Antennas and Propagation*, Vol. 16, No. 2, 172–175, 1968.

[8] Ruf, C. S., "Numerical annealing of low-redundancy linear arrays," *IEEE Transactions on Antennas and Propagation*, Vol. 41, No. 1, 85–90, 1993.

[9] Dong, J., Q. Li, R. Jin, Y. Zhu, Q. Huang, and L. Gui, "A method for seeking low-redundancy large linear arrays in aperture synthesis microwave radiometers," *IEEE Transactions on Antennas and Propagation*, Vol. 58, No. 6, 1913–1921, 2010.

[10] Jang, C.-H., F. Hu, F. He, J. Li, and D. Zhu, "Low-redundancy large linear arrays synthesis for aperture synthesis radiometers using particle swarm optimization," *IEEE Transactions on Antennas and Propagation*, Vol. 64, No. 6, 2179–2188, 2016.

[11] Dong, J., Q. Li, R. Shi, L. Gui, and W. Guo, "The placement of antenna elements in aperture synthesis microwave radiometers for optimum radiometric sensitivity," *IEEE Transactions on Antennas and Propagation*, Vol. 59, No. 11, 4103–4114, 2011.

[12] Zhu, D. and X. Peng, "Combinatorial design of low-degradation linear arrays in interferometric aperture synthesis radiometers," *IEEE Transactions on Antennas and Propagation*, Vol. 67, No. 12, 7340–7347, 2019.

[13] Zhu, D., L. Wu, Y. Cheng, and H. Lu, "Deterministic array configurations for radiometric sensitivity optimization in microwave interferometric radiometers," *IEEE Transactions on Geoscience and Remote Sensing*, Vol. 60, 1–12, 2022.

[14] Zhu, D., P. Tang, H. Lu, L. Lang, and F. Hu, "System reliability optimization of thinned linear arrays in interferometric aperture synthesis radiometers," *IEEE Antennas and Wireless Propagation Letters*, Vol. 20, No. 8, 1374–1378, 2021.

[15] Zheng, T., F. Hu, L. Wu, J. Su, and H. Hu, "Synthesis of large alias-free field-of-view linear arrays for synthetic aperture interferometric radiometers," *IEEE Transactions on Antennas and Propagation*, Vol. 68, No. 12, 7916–7926, 2020.

[16] Zhu, D., F. Hu, F. He, L. Wu, J. Li, and C.-H. Jang, "A novel optimal design of antenna array in aperture synthesis radiometers," *IEEE Antennas and Wireless Propagation Letters*, Vol. 14, 1227–1230, 2015.

[17] Scigliano, M., C. Sciannella, S. D'Addio, P. Angeletti, and G. Schettini, "Analysis of baseline redundancy in synthetic aperture interferometric radiometers," *Electronics Letters*, Vol. 46, No. 20, 1361–1362, 2010.

[18] Budé, R. X. F., T. A. H. Bressner, M. N. Johansson, M. V. Ivashina, A. B. Smolders, and U. Johannsen, "A system-performance-based comparison of sparse regular and irregular antenna arrays for millimeter-wave multi-user MIMO base stations," *Electronics*, Vol. 11, No. 3, 335, 2022.

[19] Tanner, A., T. Gaier, W. Imbriale, P. Kangaslahti, B. Lambrigtsen, and B. Lim, "A dual-gain design for the geostationary synthetic thinned array radiometer," *IEEE Geoscience and Remote Sensing Letters*, Vol. 11, No. 8, 1340–1344, 2014.

[20] Zhu, D., J. Tao, J. Su, and F. Hu, "BlockMFRAs: Block-wise multiple-fold redundancy arrays for joint optimization of radiometric sensitivity and angular resolution in interferometric radiometers," *IEEE Transactions on Geoscience and Remote Sensing*, Vol. 62, 1–15, 2024.

[21] Shami, T. M., S. Mirjalili, Y. Al-Eryani, K. Daoudi, S. Izadi, and L. Abualigah, "Velocity pausing particle swarm optimization: A novel variant for global optimization," *Neural Computing and Applications*, Vol. 35, No. 12, 9193–9223, 2023.

[22] Chen, J., Y. Li, J. Wang, Y. Li, and Y. Zhang, "An accurate imaging algorithm for millimeter wave synthetic aperture imaging radiometer in near-field," *Progress In Electromagnetics Research*, Vol. 141, 517–535, 2013.

[23] Beck, A. and M. Teboulle, "A fast iterative shrinkage-thresholding algorithm for linear inverse problems," *SIAM Journal on Imaging Sciences*, Vol. 2, No. 1, 183–202, 2009.

[24] Kennedy, J. and R. Eberhart, "Particle swarm optimization," in *Proceedings of ICNN'95 — International Conference on Neural Networks*, Vol. 4, 1942–1948, Perth, WA, Australia, 1995.

[25] Zhu, D., F. Hu, L. Lang, P. Tang, X. Peng, and F. He, "Double difference bases and thinned arrays with twofold redundancy," *IEEE Transactions on Antennas and Propagation*, Vol. 65, No. 12, 7366–7371, 2017.